



# 1 Insights into the interaction of a shale with CO<sub>2</sub>

2 Eleni Stavropoulou<sup>1,\*</sup> and Lyesse Laloui<sup>1</sup>

3 <sup>1</sup>Ecole Polytechnique Fédérale de Lausanne (EPFL), Laboratory for Soil Mechanics  
4 (LMS), EPFL-ENAC-LMS, Station 18, CH-1015 Lausanne, Switzerland

5 \*eleni.stavropoulou@epfl.ch

## 6 Abstract

7 Caprock formations such as shales, play a key role to safe underground CO<sub>2</sub> storage since they  
8 serve as a hydromechanical barrier that prevents migration of the injected CO<sub>2</sub> to the surface.  
9 While their hydromechanical response is important to ensure their sealing capacity, interaction  
10 with the injected CO<sub>2</sub> involves additional thermo-chemo-mechanical (THMC) phenomena that  
11 may threaten the long-term caprock's integrity. The low transport properties of shales make them  
12 a suitable caprock material, but at the same time challenging to study due to the very long time  
13 scales that are required for the various thermo-hydro-chemo-mechanical processes to manifest. In  
14 this work, the multiphysical interaction of the Opalinus Clay shale with CO<sub>2</sub> is studied with live  
15 x-ray tomography. Long-term exposure to liquid and supercritical CO<sub>2</sub> targets the investigation  
16 of different occurring THMC processes locally and globally in 3D that are often indistinguishable  
17 with conventional lab testing protocols. To improve spatial and temporal resolution while applying  
18 realistic pressure and temperature conditions, small size samples are studied. Long-term injection  
19 of liquid CO<sub>2</sub> resulted to a significant fissuring of calcite-rich zones that were for the first time  
20 visualised and quantified from the x-ray images, while a re-arrangement of the pre-existing micro-  
21 fissures in the clay matrix were observed. The volumetric response during direct exposure of an  
22 Opalinus Clay sample to supercritical CO<sub>2</sub> revealed an initial swelling at pre-cracked zones and  
23 initiation of new micro-fissures at areas of direct contact with the anhydrous CO<sub>2</sub> due to pore



24 water evaporation. Advanced 3D image analysis showed an increasing CO<sub>2</sub> uptake with time the  
25 elevated value of which after pressure release suggests potential CO<sub>2</sub> trapping the material.

## 26 **1 Introduction**

27 Geological CO<sub>2</sub> Storage (GCS) is an efficient way to permanently store large volumes of captured  
28 CO<sub>2</sub> by subsurface injection at pressures higher than its critical phase point ( $P_{cr} = 7.4$  MPa) where  
29 it changes from gaseous to liquid state and above a certain temperature level ( $T_{cr} = 31.2^{\circ}\text{C}$ ) to su-  
30 percritical. This relatively high pressure level strongly encourages the selection of deep reservoirs  
31 (min. 700-800 m depth), where the *in-situ* water/brine pressure equilibrates the injected CO<sub>2</sub> pres-  
32 sure. According to the most recent IPCC report (IPCC, 2022), Carbon Capture and Storage (CCS) is  
33 key to reaching net-zero emissions by mid-century and mitigating climate change. Besides, the need  
34 to implement CCS in a range of sectors including energy production, manufacturing and industry is  
35 underlined in the same report.

36 The feasibility of the technology relies on successful long-term subsurface storage which depends  
37 – at least during the first few decades – on the performance of nearly impermeable geological for-  
38 mations (seal/caprock) that will prevent CO<sub>2</sub> migration to the surface. Caprock formations, typically  
39 shales or tight mudrocks, are highly heterogeneous with low mass transfer properties, and their prone  
40 response to Thermo-Hydro-Chemo-Mechanical (THMC) loads remains a complex subject that de-  
41 serves further inquiry.

42 Shales have been studied since decades by the oil and gas industry, more recently for their use as  
43 geological barriers for nuclear waste storage, but full understanding of their suitability for geological  
44 CO<sub>2</sub> storage is still somewhat limited, since CO<sub>2</sub> injection further complexifies an already difficult  
45 engineering problem: (i) Unlike oil or water, CO<sub>2</sub> diffusion results in acidification of the *in-situ* brine  
46 that can lead to chemical interactions in the caprock and alteration of its mechanical and transport  
47 properties (Yang *et al.*, 2022); (ii) CO<sub>2</sub> injection introduces stress state changes in both the reservoir  
48 and the overlaying caprock that can cause reactivation of pre-existing faults or creation of new fracture  
49 systems (Vilarrasa *et al.*, 2019).

50 Significant progress in experimental data collection has been achieved in various scales (Armitage  
51 *et al.*, 2010; Houben *et al.*, 2013), related to both geomechanical response (Rutqvist, 2012; Wang and



52 Tokunaga, 2015; Kivi *et al.*, 2022) and chemical interactions (Wollenweber *et al.*, 2010; Hadian and  
53 Rezaee, 2020) during exposure to CO<sub>2</sub>-rich fluids. Shales are anisotropic and highly heterogeneous  
54 at different scales (micro to macro) with strong geomechanical and geochemical couplings that often  
55 challenge our ability to distinguish the different occurring phenomena and estimate their time-scale  
56 during CO<sub>2</sub> exposure.

57 In recent years, the Opalinus Clay shale has been studied as a potential caprock in the context of  
58 geological CO<sub>2</sub> storage (Amann *et al.*, 2013; Favero *et al.*, 2016; Makhnenko *et al.*, 2017; Sciandra *et*  
59 *al.*, 2021), thanks to favourable properties such as low porosity (< 20%), low permeability (in the order  
60 of 10<sup>-20</sup> m<sup>2</sup>), high clay content (40-80%), swelling properties and high sealing capacity (Marschall  
61 *et al.*, 2005; Crisci *et al.*, 2019; Delage and Belmokhtar, 2022). These favourable properties of  
62 Opalinus Clay (and shales more generally) make it a challenging material to study due to the slow  
63 flow processes at resolutions that may fall within the measurement error (Minardi *et al.*, 2021).

64 Representative testing of shales remains a big issue. Representative boundaries do not only in-  
65 volve applied pressure or temperature but also the spatial and temporal scale of the measurement.  
66 While large scale experiments are generally considered to be more realistic, they can be challenging  
67 to properly monitor and analyse since they involve the combination of multiple phenomena occurring  
68 under different scales, in particular in heterogeneous materials such as shales. A real scale exper-  
69 imental campaign has been recently completed at the Underground Research Laboratory (URL) in  
70 Mont Terri, where CO<sub>2</sub>-rich brine has been injected in an existing fault in Opalinus Clay (Zappone  
71 *et al.*, 2021). The results have not been conclusive, given the low applied pressure, the volume of  
72 injected CO<sub>2</sub> and the long time-duration required for transport phenomena to manifest in that scale.  
73 In parallel, recent lab-scale experimental results from CO<sub>2</sub> injection tests in Opalinus samples do not  
74 show evidence of significant influence on the material's basic properties for the given test duration  
75 (Minardi *et al.*, 2021; Favero & Laloui, 2018); grain density, dominant entrance pore size and void  
76 ratio, as well as hydraulic conductivity do not vary in a considerable way after exposure to CO<sub>2</sub> over  
77 a weekly time-scale. The short duration of these tests together with the chosen sample size could be  
78 among the reasons for the absence of measurable evolution.

79 Representative testing conditions and duration are even more challenging when processes of geo-  
80 chemical nature are investigated. Indeed, the impact of chemical reactivity of shales in the presence



81 of CO<sub>2</sub> remains a very challenging topic. While shales contain minerals reactive to CO<sub>2</sub>, current  
82 lab measurements are not enough since they rely either on *post-mortem* analysis of fluid compo-  
83 sition or mineralogy (Armitage *et al.*, 2013; Elkady and Kovscek, 2020). The indirect interpreta-  
84 tion of permeability results before and after CO<sub>2</sub> exposure in terms of chemical alterations (disso-  
85 lution/precipitation) can be ambiguous since they may involve self-compensating mechanisms such  
86 as carbonate dissolution, mechanical crushing and inelastic compaction as shown by various authors  
87 who studied fractured caprock samples (Yasuhara *et al.*, 2011; Hashemi and Zoback, 2021). It is  
88 thus difficult to build solid conclusions on their impact on the structural properties of the material and  
89 hence transport and mechanical response.

90 Taking all the above into account, there is a series of issues when testing shales in the context of  
91 CO<sub>2</sub> storage: (i) Flow is extremely slow resulting in long testing durations; (ii) Measured permeability  
92 variations are close to the measurement error; (iii) Reproduction of real site conditions is crucial since  
93 injection pressure and therefore effective stress has an important impact on properties of the material  
94 that drive flow and breakthrough, *i.e.* connected porosity; (iv) Chemical interactions are limited by the  
95 slow transport properties (v) The testing duration and scale that are commonly used are not enough  
96 to allow investigation in that direction.

97 In this work, the different coupled processes and phenomena that occur when CO<sub>2</sub> interacts with  
98 a shaly caprock material – the Opalinus Clay – are explored based on a series of measurements and  
99 observations from *real time* x-ray tomography. Taking full advantage of this non destructive tool,  
100 new aspects and results are targeted and demonstrated that aim to improve our understanding of the  
101 caprock's response while under realistic testing conditions. The originality of the presented research  
102 relies on the study of smaller size samples where observation period is expected to be shorter, and most  
103 importantly the direct measurement of strain fields and structural alteration from the analysis of the  
104 3D tomographic images. In the following, the proposed methodology, tools and analysis conventions  
105 are presented in detail. The results of two experimental campaigns where Opalinus Clay shale is  
106 exposed to either liquid or supercritical CO<sub>2</sub> are presented and discussed. These experiments target  
107 different coupled mechanisms that combined aim to contribute to a more profound understanding of  
108 the overall THMC response of shales with CO<sub>2</sub>.



## 109 **2 Methodology, Tools and Analysis Principles**

110 Shales are highly heterogeneous and anisotropic materials, sensitive to thermo-hydro-mechanical  
111 variations and with strong multiphysical couplings and very slow transport properties (Mohajerani *et*  
112 *al.*, 2014; Favero *et al.*, 2016; Menaceur *et al.*, 2016; Li and Laloui, 2017). Inevitably, representative  
113 testing of shales requires the employment of methods and tools that can embrace these particularities  
114 by means of controlled applied conditions and *full-field* measurement, *i.e.* a field record of a quan-  
115 tity (*e.g.*, deformation, density, temperature, *etc.*) as opposed to point-wise data (Viggiani and Hall,  
116 2008).

117 Taking into account all the above, the exploration of a new approach in testing shales with *in-situ*  
118 x-ray tomography is motivated. In this study, the full-field of micro-structural variations and kinemat-  
119 ics of the Opalinus Clay shale when exposed to CO<sub>2</sub> under different boundary conditions are targeted  
120 with 3D image analysis of real-time x-ray tomographies. Long-duration exposure of Opalinus Clay  
121 to injected liquid CO<sub>2</sub> (8 MPa) under confined conditions (10 MPa) aims to reveal potential chemo-  
122 mechanical processes, while direct exposure of unjacketed Opalinus Clay to supercritical CO<sub>2</sub> targets  
123 the better understanding of localised THM interactions that are otherwise difficult to detect with con-  
124 ventional lab-testing techniques.

125 Despite the classic testing approaches on centimetric size shale samples in the literature, in this  
126 work very small samples (5 mm) are studied in order to first gain in temporal resolution (partly in-  
127 spired by small-scale permeability testing equipment (Birmipilis *et al.*, 2019; Birmipilis and Dijkstra,  
128 2021), but also to optimise the quality of x-ray imaging (improved spatial resolution). This approach  
129 is challenging for the given material and the given subject; the pore size of shales is in the order  
130 of nanometres and thus impossible to visualise with x-ray micro-tomography (micrometric scale).  
131 Nonetheless, observation and quantification of microstructural modifications due to CO<sub>2</sub> can be ex-  
132 plored with relatively high scanning resolutions (5-8  $\mu\text{m}/\text{px}$ ) and fast tomographies thanks to the  
133 small size of the sample.

### 134 **2.1 *In-situ* x-ray micro-tomography and experimental protocol**

135 A few authors have investigated the heterogeneity and anisotropic behaviour of shales pointing out  
136 the role of the microstructure by employing different imaging techniques (Wang *et al.*, 2013; Desbois



137 *et al.*, 2017; Delage & Tessier, 2021). In the case of experimental geomechanics, x-ray tomography  
138 is the most widely used technique, with a large range of results stated in literature (Viggiani *et al.*,  
139 2015; Bedford *et al.*, 2017; Vego *et al.*, 2022; Birmpilis *et al.*, 2022). The great advantage of x-  
140 ray tomography compared to other techniques for soil characterisation (*e.g.* SEM microscopy), is  
141 the possibility to identify in 3D the specimen's heterogeneity and follow its evolution in time (*in-situ*  
142 testing). This is a very powerful tool that allows a better interpretation of test results, such as measured  
143 permeability, fingering phenomena, localised deformation or structural modifications (Voltolini and  
144 Ajo-Franklin, 2020; Stavropoulou *et al.*, 2020).

145 For this study, the dual x-ray source in PIXE platform (EPFL, Switzerland) is used. Recon-  
146 structions are performed with the XAct software provided by RX-Solutions (Annecy, France), with  
147 appropriate beam-hardening corrections applied. The PEEKcell is fixed on the rotating table, as close  
148 as possible to the x-ray source, for a maximal use of the x-ray conical beam. All scans are performed  
149 in temperature controlled environment of 21°C.

150 A cylindrical cell made out of PEEK is used for the application of the various boundary conditions,  
151 that are explained in detail in the following sections. The so called PEEKcell, is designed to host  
152 5 mm × 5 mm cylindrical samples and can sustain a maximal pressure and temperature of 20 MPa  
153 and 80°C respectively (Stavropoulou and Laloui, 2022). An entry on each side of the cell (top and  
154 bottom) allows the application of confining pressure (top) and pore pressure on the sample (bottom).  
155 The cell is disconnected from the pressure controllers and transported under the given pressure state  
156 in the tomograph. To monitor the pressure level during the scans, a pressure transducer is placed on  
157 each side (see Figure 1).

158 The samples are cut to cylindrical shape of  $d = h = 5$  mm; first sized down in rectangular pieces  
159 with a saw and then reduced to the desired size manually using fine sand paper (P240). This technique  
160 has been preferred (to a mechanical lathe for example) in order to avoid overheating the sample during  
161 preparation. The resaturation of the samples has been achieved progressively under free swelling  
162 conditions by exposing the samples in a controlled relative humidity (RH) environment with the use  
163 of an appropriate saline solution (Romero, 2001); first to RH = 75% (NaCl) and then RH = 98%  
164 ( $K_2SO_4$ ) until mass stabilisation. Before testing, samples have achieved a close-to-full saturation  
165 state, corresponding to a measured water content  $w_{resat} = 6.1 - 6.8$  %, i.e. within the range of full

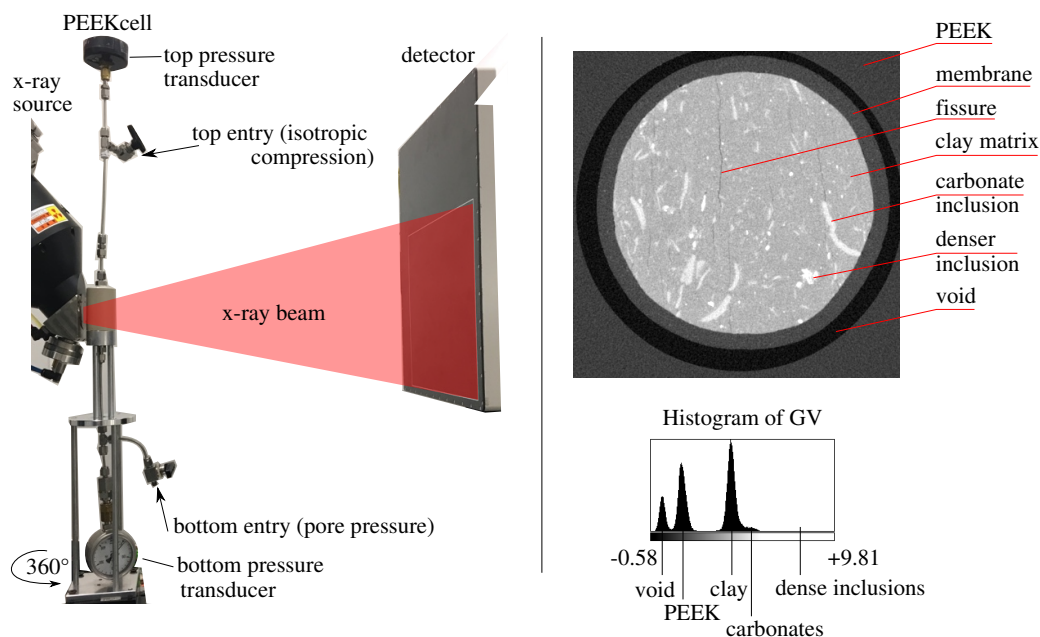


Figure 1: (left:) PEEKcell setup in the x-ray tomograph, (right:) horizontal slice of a reconstructed x-ray image and the corresponding histogram of greyvalues

166 saturation (Bossart and Thury, 2011).

167 In this work, the micro-structural modifications due to long-duration CO<sub>2</sub> exposure are investi-  
168 gated with *post-mortem* measurements and analysis, *i.e.* after removing the applied pressures. Then,  
169 the occurring kinematics on Opalinus Clay that is exposed in direct contact (no sealing membrane)  
170 with supercritical CO<sub>2</sub> is examined with *in-situ* measurements, *i.e.* while under pressure in the cell.  
171 According to the volumetric response of the sample and the corresponding GV of the images, the  
172 CO<sub>2</sub> uptake is investigated and visualised for the first time.

173 When supercritical CO<sub>2</sub> is injected, a thermal jacket is used around the cell and the applied tem-  
174 perature is monitored with a thermal sensor that is placed between the jacket and the PEEKcell. For  
175 achieving a maximal resolution and x-rays penetration the thermal jacket is removed during the scans.  
176 Inevitably, this leads to CO<sub>2</sub> phase change from supercritical (lower density) to liquid (higher density)  
177 and consequently to pressure drop under constant volume conditions, *i.e.* conditions during scanning.  
178 In order to minimise this pressure drop, the cell is exposed to the scanner's temperature (21°C) two  
179 hours in advance while maintaining the pressure at the desired level (pressure pump connected), in or-



180 der to avoid pressure loss due to phase change during the scan. The possible implications of this CO<sub>2</sub>  
181 phase transition before the scans on the given testing campaign are discussed in the corresponding  
182 section of direct exposure to supercritical CO<sub>2</sub>.

## 183 2.2 Image Analysis

184 The result of an x-ray tomography is a 3D x-ray attenuation map of the scanned sample that is asso-  
185 ciated to the 3D density map of the material. For instance dense phases in the material (*e.g.* mineral  
186 inclusions) attenuate more x-rays than lower density phases (*e.g.* cracks, pores). The different den-  
187 sity (attenuation) levels reflect in the grey level values (GV) of the reconstructed 3D x-ray image;  
188 higher GV corresponds to denser phases and lower GV to lower phases as indicated in Figure 1-right.  
189 Changes in the GV of a scanned sample in time or due to application of a different load allow the ob-  
190 servation and quantification of localised micro-structural modifications (*e.g.* crack opening/closing,  
191 swelling/shrinking) which can subsequently be translated to 3D strain fields with Digital Volume Cor-  
192 relation (DVC). In this work, the open source SPAM software (Stamati *et al.*, 2020) is used for the  
193 DVC analysis.

194 In DVC, two images are required; an initial (reference image) and a deformed one. In the case  
195 of local-DVC (that is used for the image analysis in this work), a grid with a given node spacing  
196 is defined and at each grid point a centred window is extracted. For each of these subvolumes a  
197 linear deformation function  $\Phi$  is calculated so that  $\text{im}_{\text{def}}(\Phi \cdot x) = \text{im}_{\text{ref}}(x)$ . The function  $\Phi$  accounts  
198 for translation, rotation and stretching and its calculation is optimised by solving an iterative problem  
199 that minimises error based on the classic sum of squared difference (SSQD). While DVC can calculate  
200 a strain field and that can then be applied it on an image, it does not take into account by definition the  
201 variations of the GV due to the corresponding strain. GV correction due to deformation is going to be  
202 applied in this work as per (Stavropoulou *et al.*, 2020) where the aim is to investigate phase changes  
203 due to chemical reactions between the in-contact CO<sub>2</sub> with the same material.

204 All scans of each type of test are performed under the same conditions and with the same scanning  
205 parameters. Nevertheless, noise, artefacts or other external changes may be present between the dif-  
206 ferent scans (that in some cases are performed in month intervals). To improve the accuracy of image  
207 analysis and minimise the GV variations due to measurement conditions rather than real changes in





208 the material, all images from a testing campaign are normalised based on GV of materials, the density  
209 of which is not supposed to vary between the different scans; here PEEK and aluminium. The proce-  
210 dure of the GVs normalisation is explained in detail in the Appendix and results in scaling the given  
211 images so that the voxels that correspond to void are set to  $GV = 0$  and those of PEEK correspond to  
212  $GV = 1$ .

213 Finally, for the strain field calculation, the occasional rigid-body transformation of the sample  
214 (translation and rotation) due to transportation and re-installation of the cell in the tomograph, is  
215 calculated based on the a single  $\Phi$  function on the entire image (so called registration) and removed.  
216 DVC is then performed between the reference image and the deformed ones from which rigid body  
217 motion has been corrected. The displacement field is then calculated and translated to strain assuming  
218 small transformations (see all details in Stamati *et al.*, 2020). The above principles and conventions  
219 are applied for the analysis of the different series of x-ray scans that are presented in the following.

### 220 **3 Mineralogical analysis and long-term structural modifications**

221 In this section, the long-term chemo-mechanical interactions that can occur between  $CO_2$  and a shaly  
222 caprock are explored. When  $CO_2$  is placed in contact with the pore water of the shaly caprock  
223 material, it results in acidification of the pore fluid – by means of diffusion – and therefore resulting  
224 in an alteration of the chemical equilibrium. For instance, pre-existing carbonate crystals might be  
225 dissolved by the acidic fluid and enhance the material's transport properties (Busch *et al.*, 2008;  
226 Espinoza *et al.*, 2011; Jia *et al.*, 2018). On the other hand, incorporation of supercritical  $CO_2$  in  
227 micro-structural interlayers can induce the beneficial swelling of smectitic clays (as is expected in  
228 self-sealing for nuclear storage applications), but it is not clear whether such a response would occur  
229 *in situ* since such tests have taken place under unconfined conditions (batch reactors) (Alemu *et al.*,  
230 2011).

231 Taking into account the small size of the samples ( $5\text{ mm} \times 5\text{ mm}$ ), first a mineralogical analysis  
232 of different Opalinus Clay samples is performed with x-ray diffraction (XRD) measurements, in order  
233 to evaluate the mineralogical variability. Then the mineralogical map of an Opalinus Clay sample is  
234 studied with SEM-EDX (scanning electron microscopy and energy dispersive x-ray) measurements  
235 and the identified mineral locations is directly compared and identified in the corresponding slices



236 from the x-ray tomography image of the same sample. This combined analysis aims to locate and  
237 demonstrate elements in the sample that may favour chemical interactions in the long-term presence  
238 of CO<sub>2</sub> (e.g. Ca, C, Si, S, O etc.) that is here investigated with x-ray tomography by means of  
239 occurring micro-structural modifications (fissuring, swelling, self-sealing etc.).

240 Table 1 shows the mineralogical composition of four sister Opalinus Clay samples from XRD  
241 measurements. The fit was optimised on one sample and to increase comparability, the next fits were  
242 done by keeping all refined parameters and replacing the data file on the current model. Even though  
243 the results are quite approximate, a similar quartz and clay content is measured for all samples except  
244 for illite that presents variations up to 8%. In the lower illite-rich samples a higher calcite content is  
245 measured with values that vary among the different samples from 13% to 24%. The mineral content  
246 of sample A (in bold) is measured after long-term exposure to CO<sub>2</sub>. It presents a high clay content  
247 that is unclear if it is affected in any way by its previous interaction with CO<sub>2</sub> since its overall mineral  
248 content falls within the variability of the other three *untreated* samples. Sample A is used to compare  
249 the results from all different analysis tools that are employed for this study.

| <b>Opalinus Clay (wt%)</b> | <b>A</b>    | X    | Y   | Z    |
|----------------------------|-------------|------|-----|------|
| Calcite                    | <b>21</b>   | 13   | 16  | 24   |
| Quartz                     | <b>13</b>   | 13   | 14  | 11   |
| Chlorite                   | <b>15</b>   | 15   | 13  | 17   |
| Kaolinite                  | <b>3</b>    | 2    | 2.5 | 1.5  |
| Illite                     | <b>45.5</b> | 53.5 | 52  | 45.5 |
| Siderite                   | <b>2</b>    | 2    | 2   | 11.5 |
| Pyrite                     | <b>0.5</b>  | 0.5  | 0.5 | 0.5  |

Table 1: Mineralogical composition of four sister Opalinus Clay samples based on x-ray diffraction

250 In order to confirm the mineralogy of the inclusions identified from x-ray tomography, sample A  
251 has been subjected to a SEM-EDX analysis. The height of the sample is carefully reduced to the height  
252 of the horizontal slice of Figure 2-a using again light sandpaper (the traces of which are apparent in  
253 the SEM images). Figure 2 presents the combined information obtained both from x-ray tomography  
254 and SEM-EDX at the same horizontal slice. In Figure 2 (a) the x-ray slice, the different GV levels  
255 highlight the distribution of the different inclusions in the clay matrix, the mineralogy of which is  
256 identified from the EDX analysis. In fact, there are two sets of inclusions as revealed from the GV  
257 histogram plotted in Figure 2 (b). This is more clear when a bilateral filter is applied (red histogram)



258 that unveils a second peak that represents the lower GV inclusions.

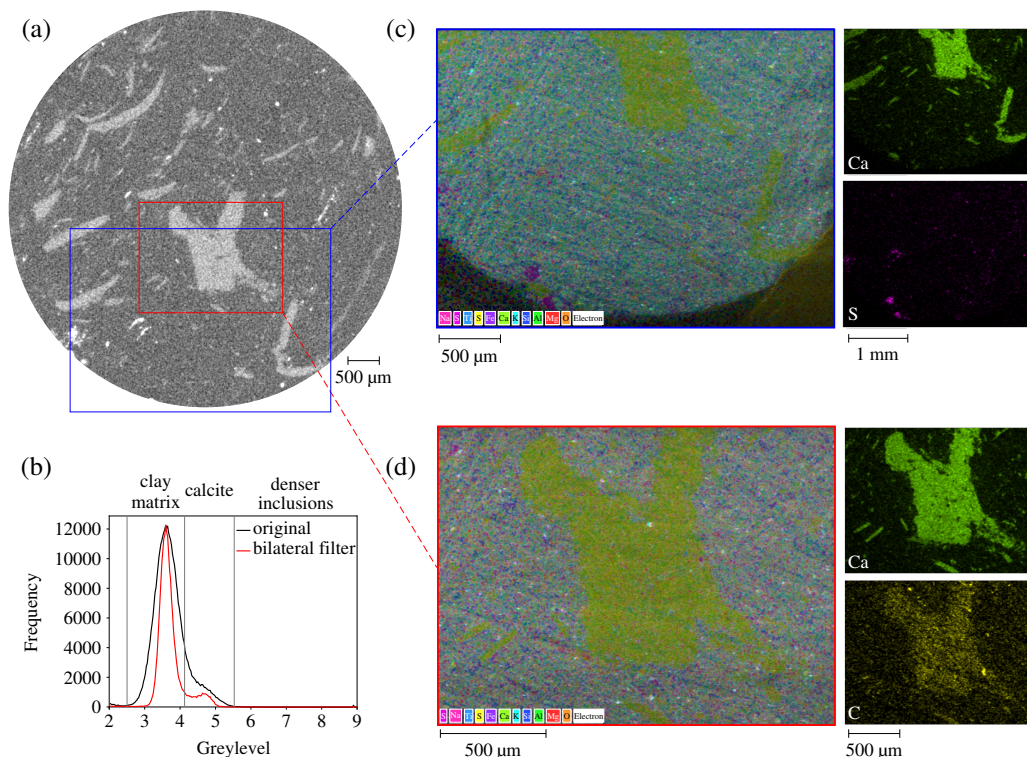


Figure 2: Identification of the inclusions' mineralogy combining x-ray tomography and SEM-EDX – (a) horizontal x-ray tomography slice, (b) histogram of GVs of the top horizontal slice, (c) SEM-EDX map corresponding to the blue window of the x-ray slice highlighting all identified elements and the areas rich in Ca and S, (d) SEM-EDX map corresponding to the red window of the x-ray slice highlighting all identified elements and the areas rich in Ca and C

259 These lower GV level inclusions are rich in calcite (Ca) and carbon (C) as revealed from the EDX  
260 images (Figure 2 (c) and (d)). This type of inclusions are therefore more prone to undergo dissolution  
261 in the presence of CO<sub>2</sub>. The denser inclusions (whiter inclusions in Figure 2 (a) at the bottom left of  
262 the sample) seem to be rich in sulphur (S) (Figure 2 (c)), a main element of pyrite (FeS<sub>2</sub>) the density  
263 of which is very high. This supplementary EDX measurement reveals that the information from the  
264 3D x-ray images is even richer than what has widely been used for now.

265 Sample A is the same sample that has been used in (Stavropoulou and Laloui, 2022); it has first  
266 been scanned in the x-ray tomograph under unconfined conditions, then after application of confine-  
267 ment (10 MPa) followed by CO<sub>2</sub> injection up to 8 MPa (pixel size 7.8 μm). After CO<sub>2</sub> breakthrough,



268 it has been let under constant volume conditions in the PEEKcell for 9 months and scanned again in  
269 the x-ray tomograph after pressure release (same pixel size and scanning parameters). It is important  
270 to mention that there has been pressure loss during these 9 months that has not been properly moni-  
271 tored. Nevertheless, the results present great interest that is not necessarily impacted by this pressure  
272 loss.

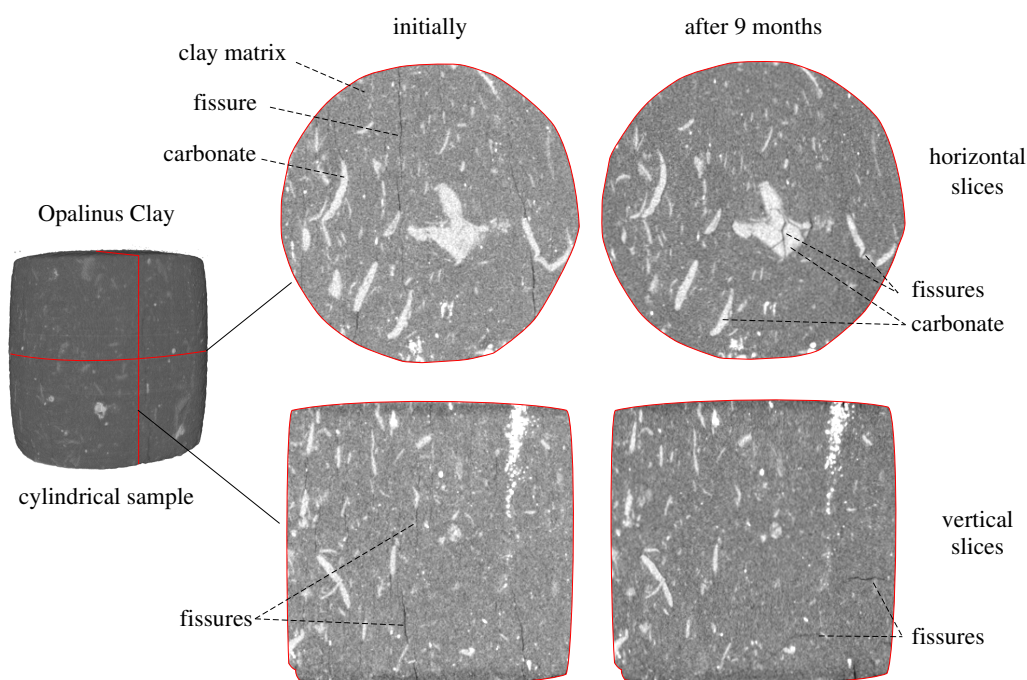


Figure 3: Horizontal and vertical slices of x-ray tomography on the same Opalinus Clay sample with highlighted fissures (in black) under unconfined conditions at its initial state (left) and after 9 months CO<sub>2</sub> exposure (right). The horizontal slices (top) highlight the fissuring of the carbonate phase due to dissolution and the self sealing of the clay matrix pre-existing fissures under long-term confinement; the vertical slices (bottom) highlight the fissure rearrangement and change of orientation that took place in time.

273 Figure 3, shows a horizontal and vertical slice of two x-ray scans of sample A, initially and after  
274 9 months of CO<sub>2</sub> exposure, both in unconfined conditions. The micro-fissures have been manually  
275 highlighted in black for more clarity, but the entire volumes can be found at their original form in  
276 the supplementary material. The initial image of the sample reveals a vertical bedding orientation  
277 according to the orientation of the pre-existing fissures in the clay matrix. After 9 months of CO<sub>2</sub>  
278 exposure there are two important observations to be pointed out. First, clear fissures in the carbonate



279 phases have been formed revealing the calcite dissolution for the first time from x-ray images and  
280 under non-extreme (if not realistic) testing conditions. In addition to the fissuring of the carbonate  
281 inclusions, a disappearance of the initially pre-existing fissures in the clay matrix is observed. This can  
282 be explained first by means of self-sealing behaviour of the material under long-duration application  
283 of confinement and then by precipitation of Si-rich zones that are not distinguishable from the x-ray  
284 images, since they have similar density with the clay minerals. Indeed, (Prakash *et al.*, 2022) pointed  
285 out a more pronounced precipitation activity in zones parallel to the direction of the bedding plane.

286 For a better understanding of the micro-structural modification of the sample after long-term CO<sub>2</sub>  
287 exposure, the orientation of the minimum eigenvectors (longest axis) of the inclusions and micro-  
288 fissures have been plotted in 3D together with their projection in the 2D plane, as shown in Figure 4.  
289 Both types of orientation plots are presented for a better demonstration of the result of each studied  
290 phase – the 3D histogram is more comprehensible for the cracks' orientation and the 2D projection for  
291 the inclusions. For this analysis, a bilateral filter has been applied on the two images to reduce noise  
292 and to smoothen the edges between the different phases (clay/cracks, clay/inclusions). In this way a  
293 better segmentation of the phases of interest (cracks and inclusions) can be achieved. It is known that  
294 segmentation of shale images remains a difficult task due to the heterogeneity and the contrast of the  
295 different phase interfaces. Even though these results could be optimised from a quantitative point of  
296 view, the overall shape modification of the two segmented phases is realistic.

297 The 2D projection of the min. eigenvectors of the inclusions reveals a preferential orientation  
298 along the vertical axis – axis parallel to the bedding plane – both initially and after 9 months exposure  
299 (Figure 4). The vertical axis of the 2D plots is parallel to the Y axis of the spherical histograms that are  
300 plotted in this view to demonstrate the vectors' orientation on the ZY plane. After 9 months exposure  
301 to CO<sub>2</sub> the population of inclusions is increased as demonstrated by both plots on the right of Figure 4.  
302 This increase in the number of inclusions is a clear indication of carbonate dissolution that resulted in  
303 inclusion fissuring and consequently identification of more numerous inclusion *particles*. The main  
304 orientation axis after dissolution remains vertical, suggesting that fissuring due to dissolution has  
305 mainly occurred along the shortest axis of the inclusions and therefore perpendicularly to the bedding  
306 plane.

307 In a similar way, the spherical histograms of the minimum eigenvector of the sample's identified

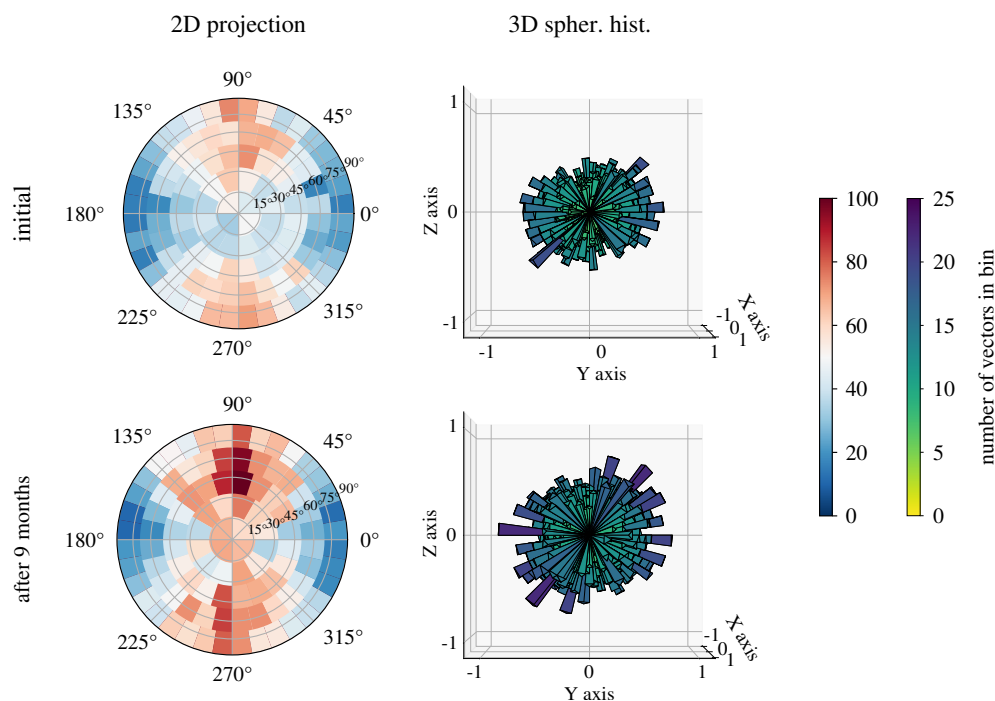


Figure 4: 2D projection (left) and spherical histogram (right) of the minimum eigenvectors of sample's O<sub>2</sub> inclusions, initially and after 9 months exposure to CO<sub>2</sub>

308 cracks and their 2D projection are plotted in Figure 5; initially and after 9 months of CO<sub>2</sub> exposure.  
309 The shape of the 3D histogram initially reveals the sample's anisotropy with a preferential orientation  
310 parallel to the bedding plane. This is confirmed by the high number of vectors projected on the vertical  
311 axis of the 2D plot – even though the low number of cracks make it harder to evaluate. Interestingly,  
312 the shape of the cracks' 3D histogram on the right is very different, confirming the observations  
313 and assumptions discussed from Figure 3. First, the number of cracks is reduced, validating the  
314 self-sealing (or precipitation) response of the sample after long-duration confinement. Then, most  
315 importantly, the orientation of the main cracks has been totally modified and is no more parallel  
316 to the bedding. It is not clear whether these new fissures are the result of alteration of the pore  
317 fluid's pH that enhances further chemical reactions between minerals that are not detectable from  
318 x-rays and CO<sub>2</sub>, or whether they are related to mechanical impact from CO<sub>2</sub> breakthrough (see 3D  
319 volumetric response after breakthrough in Stavropoulou and Laloui, 2022). In either case, this result  
320 points out a potential rearrangement of the fissure network after long-term CO<sub>2</sub> exposure that has not

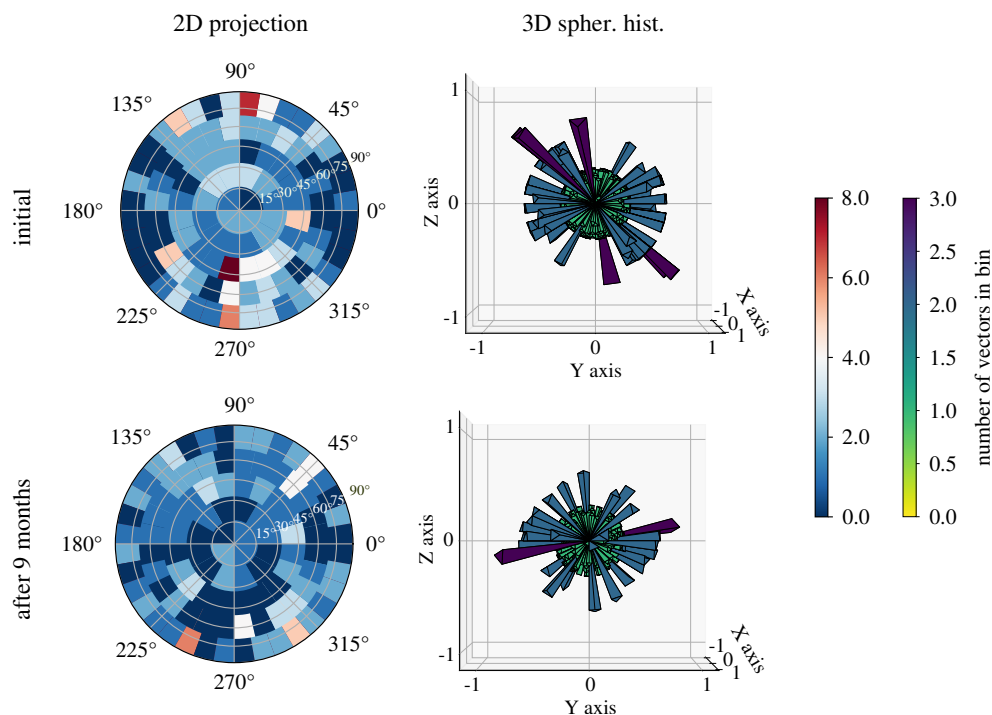


Figure 5: Spherical histogram of the minimum eigenvector of the inclusions and the cracks in sample A, initially and after 9 months exposure to CO<sub>2</sub> (colour represents the number of projected points per bin divided by the median number of points in all bins)

321 been previously discussed. Most importantly, these results show how little we still know regarding  
322 the coupled long-term THMC response of the caprock/CO<sub>2</sub> interaction at the micro-scale and their  
323 implications to the large scale response. Longer-duration testing under realistic boundary conditions  
324 are required for a better understanding of the complex mechanisms that occur.

325 Finally, in the aim of a better visualisation of the texture of the carbonic inclusions, the SEM  
326 image of the same (unpolished) slice with Figure 2 is presented in Figure 6. For the SEM images,  
327 two detectors have been used; (top) a secondary elements detector that basically illustrates the sur-  
328 face topography; and (bottom) a backscattered electrons detector that shows a Z contrast, *i.e.* lighter  
329 elements (such as Si, Al, O, K) are darker and heavier elements (here Ca or C) are brighter. The  
330 secondary elements detector does not reveal any information regarding the targeted inclusion other  
331 than the fewer sandpaper traces that are very obvious on the softer clay matrix. On the other hand,  
332 the backscattered electrons detector provides a better distinction between the two phases. The higher

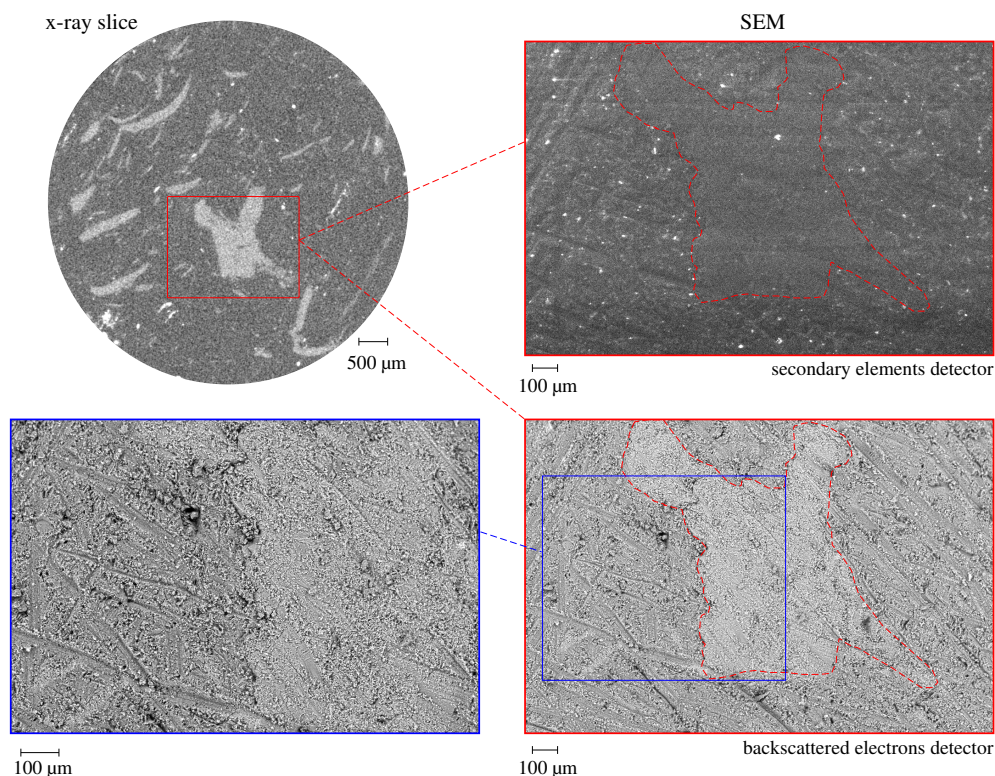


Figure 6: Opalinus Clay core sample

333 resolution of SEM allows a better visualisation and understanding of the interface between the car-  
334 bonate inclusion and the clay matrix that is otherwise not visible with x-rays. While the resolution  
335 is still in the micrometric scale and no nanometric pores can be detected in either types of images,  
336 a distinct calcite/clay interface of increased porosity is revealed in the zoomed area of the bottom  
337 SEM image (blue window). Indeed, this is a good confirmation of what is reported in (Minardi *et*  
338 *al.*, 2021) carbonate-rich Opalinus Clay; the pore size distribution is bimodal with a second dominant  
339 pore size between 50-100  $\mu\text{m}$  corresponding to the interface of carbonate/clay particles. This high  
340 inter-particle porosity can serve as a preferential  $\text{CO}_2$  pathway and eventually enhance geochemical  
341 interactions; in this case carbonate dissolution.





## 342 **4 Direct exposure to supercritical CO<sub>2</sub>**

343 In this part, the interaction of an Opalinus Clay sample with supercritical CO<sub>2</sub> is evaluated in time by  
344 means of quantitative 3D x-ray image analysis. The unjacketed caprock sample is exposed from all  
345 sides (equilaterally) to direct contact with supercritical CO<sub>2</sub> (p = 10 MPa and T = 34°C) and regular  
346 x-ray scans (resolution 5.38 μm) are performed for the study of its volumetric and micro-structural  
347 response. The water saturated sample is mounted in the PEEKcell and a first scan (00) is performed  
348 under initial ambient unconfined conditions. Then, the target pressure and temperature are applied  
349 and the sample is let to interact with the in-contact CO<sub>2</sub>. Further scans of the sample are performed  
350 while under pressure in the PEEKcell after 13 days (scan 01), 30 days (scan 02) and 56 days (scan  
351 03), as well as after release of pressure and temperature (scan 04).

### 352 **4.1 Volumetric response**

353 The 3D volumetric response of the caprock material under the above mentioned conditions are evalu-  
354 ated and quantified by means of DVC analysis. As explained earlier, to properly compare and analyse  
355 the acquired images, the occasional rigid-body transformation (translation and rotation) is removed  
356 so that the images are well aligned as shown in the left column of Figure 7. The middle vertical slice  
357 of the tested sample reveals the pre-existence of 3 principal fissures parallel to each other and parallel  
358 to the bedding orientation of the sample, *i.e.* perpendicular to the vertical axis of the sample. These  
359 micro-fissures of initial max. aperture ≈ 30 μm may have been induced during sample preparation  
360 and/or during resaturation under free swelling conditions. Their existence is not necessarily an is-  
361 sue for the given study; on the contrary they can provide important insight into the impact of their  
362 presence upon interaction with CO<sub>2</sub>. Looking more closely at the microstructure of the middle slice  
363 in Figure 7 an increase of the bottom principal pre-existing fissure can be observed, as well as the  
364 creation and propagation of additional new micro-fissures at the bottom of the sample; between the  
365 bottom left inclusion structure and the lower principal fissure.

366 For a more quantitative analysis of the localised response of the sample, the volumetric strain  
367 is calculated in 3D between each scan and the initial state of the sample (scan 00) that is used as  
368 reference. For the DVC analysis, the chosen parameters (half window size, node spacing *etc.*) are  
369 detailed with the additional provided data online. The map of the calculated volumetric strain of each

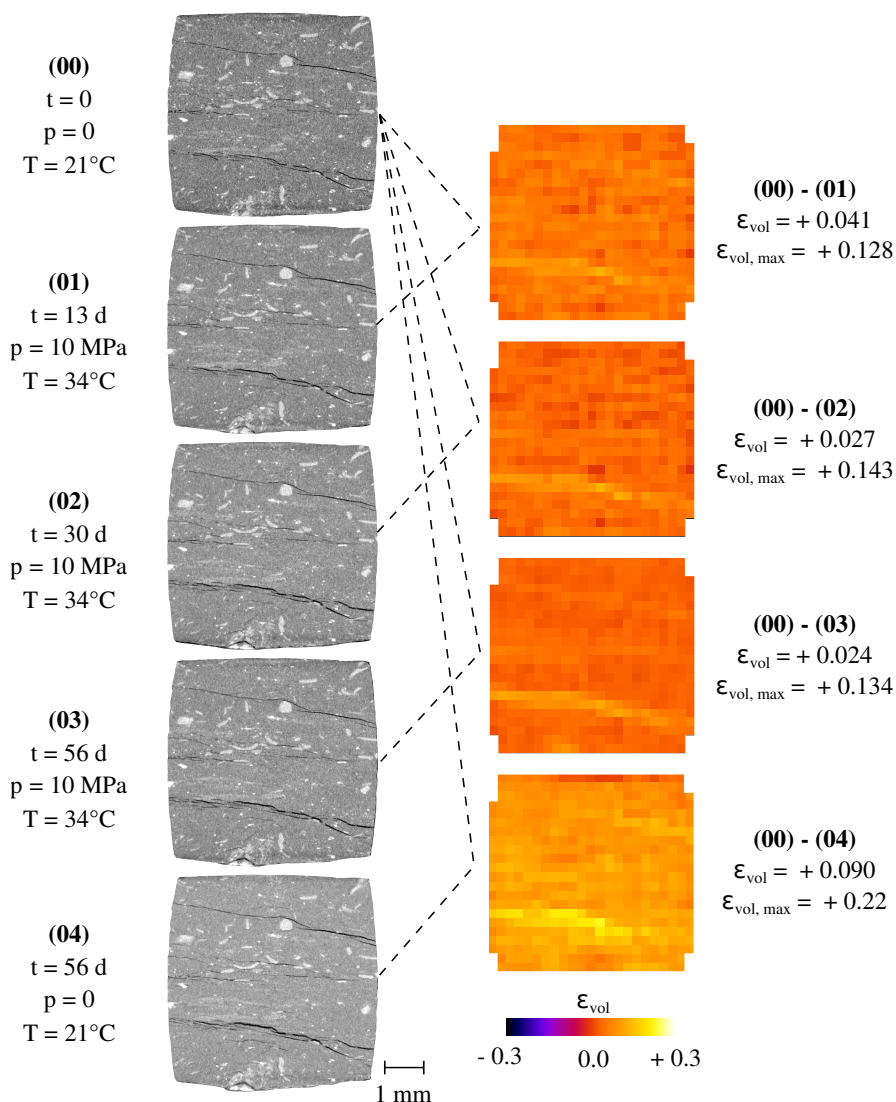


Figure 7: Volumetric response of the middle vertical slice of the Opalinus Clay sample in time after exposure to supercritical CO<sub>2</sub>

370 scan presented on the right column of Figure 7 where the corresponding middle vertical slice is shown  
 371 – it must be noted that the values of measured volumetric strain, total ( $\epsilon_{vol}$ ) and maximum ( $\epsilon_{vol,max}$ )  
 372 correspond to the entire 3D volume. In all scans a more pronounced expansion is measured on the  
 373 location of the lowest pre-existing micro-fissure ( $\epsilon_{vol,max}$ ). Only after 2 months of CO<sub>2</sub> exposure (scan  
 374 03) a slight expansive activity may be measured around the other two pre-existing ones. The overall



375 expansive response of the sample (positive  $\epsilon_{vol}$ ) is clearly dominated by the expansion of the fissures  
376 that remains mostly constant in time For the rest of the material it is hard to observe a clear pattern,  
377 nevertheless the calculated volumetric strain reveals an initial expansion ( $\epsilon_{vol00-01} = + 0.041$ ) that in  
378 time reduces ( $\epsilon_{vol00-02} = + 0.027$ ) and stabilises ( $\epsilon_{vol00-03} = + 0.024$ ). Finally, upon pressure decrease,  
379 the material expands in a pronounced way ( $\epsilon_{vol00-03} = + 0.090$ ) not only at the lower crack zone but  
380 everywhere in the sample due to stress relaxation, as explained in the following.

381 The interpretation of this response is not straightforward since the sample is subjected to complex  
382 THMC boundary conditions. In theory, the application of constant pressure equilaterally and directly  
383 in contact with a fully water saturated sample is not supposed to affect the applied effective stress  
384 that should remain zero. In other words, since  $CO_2$  is *injected* equilaterally in the unjacketed sample,  
385 the concept of effective stress is not valid, neither is the concept of hydraulic fracturing with the  
386 increase of pore pressure as it is the same with the applied skeleton pressure. However, the presence  
387 of pre-existent fissures suggests that the sample cannot be realistically fully saturated and there matric  
388 suction must be present locally in the fissured and partially saturated zones. Upon high pressure  $CO_2$   
389 exposure suction breakdown occurs locally (decrease of effective stress) and the sample swells until  
390 stabilisation at full saturation – water +  $CO_2$ . This interpretation can confirm the initial volumetric  
391 activity that eventual stabilises in time.

392 Local modification of the effective stress is not the only mechanism that may take place upon  
393 exposure of a shale sample to supercritical  $CO_2$ . Temperature increase ( $34^\circ C$ ) induces thermal ex-  
394 pansion to the sample that can indeed justify the rather isotropic expansion measured in scan 01.  
395 Another important aspect that has been little discussed in the literature is the dessication of the ma-  
396 terial when in contact with  $CO_2$ . Indeed, the pore water of the material evaporates in the anhydrous  
397  $CO_2$  resulting desaturation which can result to further crack opening (expansion) and pore collapse  
398 in the clay matrix. This dessication effect could explain the lower volumetric expansion in time until  
399 eventual equilibrium. This little discussed interaction can occur in real field conditions at the bot-  
400 tom of the caprock formation in contact with the buoyant  $CO_2$ , leading to partial desaturation of the  
401 caprock and threaten its mechanical integrity and sealing capacity.

402 To better understand the impact of the afore mentioned coupled THM mechanisms, the evolution  
403 of the fissures' volume in the different scans is presented in Figure 8. For their calculation the same

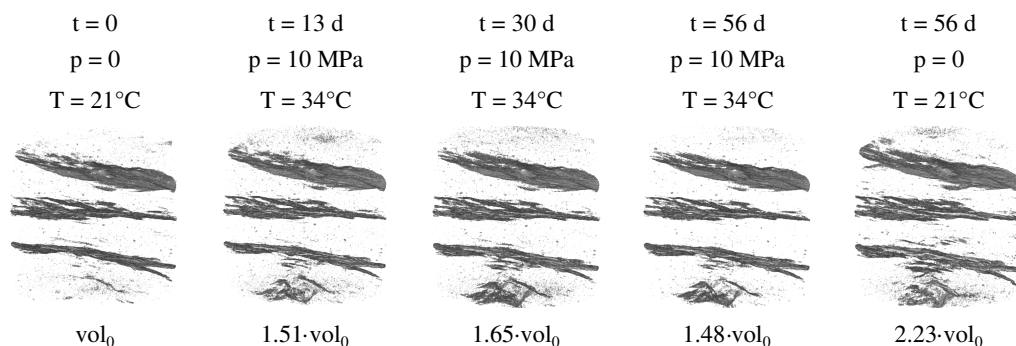


Figure 8: Evolution of pre-existing fissures and appearance of new ones after direct exposure to supercritical CO<sub>2</sub> (illustration in 3D)

404 GV threshold has been used for all the normalised scans. Once again, segmentation of shale images  
405 is a difficult exercise, the optimisation of which is out of the scope of this study. The obtained results  
406 are considered sufficient to demonstrate the overall behaviour of the material. While the volumetric  
407 increase of the pre-existing fissures has already been identified from the calculated volumetric maps  
408 of the entire sample, Figure 8 clearly demonstrates the creation and propagation of a new family  
409 of fissures at the bottom of the sample. These new fissures demonstrate in a very clear way the  
410 dessication effect of anhydrous CO<sub>2</sub> explained above. Additional chemo-mechanical mechanisms  
411 may contribute to the initiation of these micro-fissures that are impressively localised in a calcite-rich  
412 area at the bottom of the sample (see x-ray images in Figure 7). Eventual dissolution aspects are hard  
413 to interpret since preferential fissuring patterns in calcite-rich zones may primarily be due to increased  
414 porosity between the calcite and the clay mineral interface (as shown in Figure 6).

## 415 4.2 CO<sub>2</sub> uptake

416 After the in-depth analysis of the microstructural response of the caprock material during direct con-  
417 tact with supercritical CO<sub>2</sub>, an attempt to visualise and quantify the CO<sub>2</sub> penetration in the material  
418 is attempted in this part of the study. The analysis is based on the evolution of the x-ray images' GVs  
419 after correction due to volumetric strain as per (Stavropoulou *et al.*, 2020). This approach is quite  
420 ambitious in the context of CO<sub>2</sub> uptake, since the density variations due to supercritical CO<sub>2</sub> invasion  
421 are very slight. This is why normalisation of the images' GVs is imperative for this kind of analysis  
422 (see Appendix).



423 Taking into account the measured strain field from the DVC analysis, the variation of the x-ray  
424 attenuation coefficient ( $\mu_x$ ) in time is corrected and measured. Volumetric strain results in density  
425 variation (and therefore  $\mu_x$  variation) that is manifested in the GVs level of the deformed image via a  
426 linear relationship. A simple example to better understand this reasoning is the case of thermal expan-  
427 sion with no mass transfer, where the density of the material is expected to reduce, and consequently  
428 the attenuation field  $\mu_x$  or GVs to decrease proportionally to the change in density. Any additional  
429 GV variation is therefore assumed to be due to additional mass transfer (gain or loss); in this work  
430 due to CO<sub>2</sub> uptake. According to (Stavropoulou *et al.*, 2020), the attenuation variation of a sample is  
431 calculated as a function of the mechanical volumetric strain assuming mass conservation:

$$\Delta\mu = -\varepsilon_v \cdot \mu_0 \quad (1)$$

432 where  $\varepsilon_v$  is the measured volumetric strain of the sample and  $\mu_0$  is the initial attenuation of the  
433 image (before loading).

434 In order to measure the additional changes of GVs due to mass transfer, the calculated strain  
435 field is applied on the reference image (scan 00), while taking into account the corresponding GV  
436 correction. Then, simple subtraction of the deformed image (with corrected GVs due to volumetric  
437 variation) from the corresponding original image (*e.g.* 01 minus 00\_def\_to\_01) results in the uptake  
438 or loss of mass. The result of this analysis is presented in Figure 9, where the chosen colourbar  
439 represents density (in terms of GV) increase (red) or decrease (blue).

440 The maps of the GV variation show a density decrease overall during the first month of exposure  
441 (00-01 and 00-02). This response can be supported by the sample's desaturation discussed earlier; in  
442 fact, invasion of anhydrous CO<sub>2</sub> in the material partially occurs through water evaporation, therefore  
443 the material is filled up with a fluid of lower density. While these results are somewhat noisy for  
444 precise conclusions, nevertheless a more pronounced *density decrease* is obtained during the first  
445 month at the lower part of the sample where *crack initiation* occurs. On the other hand, around the  
446 zones of the *pre-existing fissures* a *density increase* is measured; in this case the non saturated zones  
447 around these fissures might have been filled in with CO<sub>2</sub>. It has to be noted that this approach is even  
448 less accurate around in the crack locations. This is because the obtained fields are the result of the  
449 subtraction between the initial least fissured image (00) with a future deformed image (*e.g.* 02) that  
450 has more fissures – the application of the calculated deformation field on 00 cannot create these new

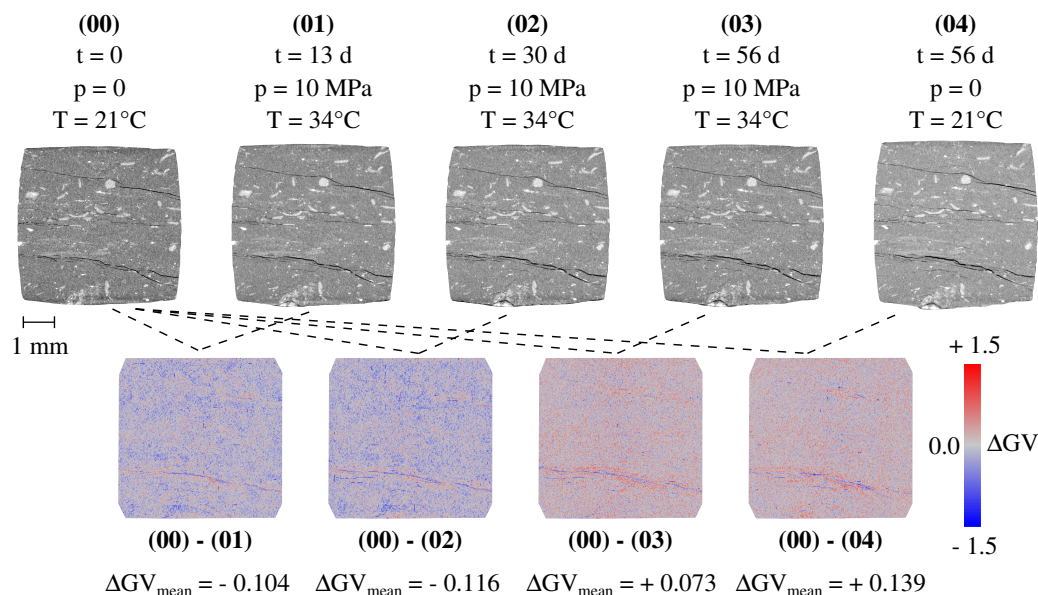


Figure 9: Fields of the grey value changes of the caprock material in time after removing the changes due volumetric strain

451 fissures this is why directly on the fissures the density will be always decreasing (blue).

452 Two months after CO<sub>2</sub> exposure, the overall density of the material eventually increases in a  
 453 relatively homogeneous way, if not with more noticeably around the lower pre-existing fissure. It is  
 454 interesting to notice that between scans 02 and 03 the volumetric activity that was measured is almost  
 455 negligible. This density increase under constant volume reveals the saturation of the material with  
 456 CO<sub>2</sub>. Indeed, unlike the previous two fields, here the material seems to be in equilibrium indicating  
 457 that CO<sub>2</sub> has invaded it in its entity. Final CO<sub>2</sub> pressure release (00-04) leaves the sample with an  
 458 overall increased density, in particular at the zones around the fissures and at the bottom. This final  
 459 result may indicate chemo-mechanical or CO<sub>2</sub> trapping phenomena that may occurred during the two  
 460 month exposure. This is a first attempt to visualise CO<sub>2</sub> invasion in a caprock material and even  
 461 though it is quantitative in terms of GV levels, their physical interpretation in terms of *e.g.* actual  
 462 CO<sub>2</sub> volume increase or water decrease requires further studies and measurement for the calibration  
 463 of the different phases' GVs.



## 464 **5 Discussion and Conclusions**

465 In this work the interaction between the Opalinus Clay, a caprock representative material, with CO<sub>2</sub>  
466 is studied with x-ray tomography imaging. The different results and observations reveal the complex  
467 response of this material due to multiple coupled phenomena that occur in parallel. Exposure to  
468 supercritical CO<sub>2</sub> implies temperature increase of the material that results in thermal expansion (TM  
469 coupling). This expansion leads to inevitable desaturation of the material (TH coupling). At the  
470 same time, the live observation of the caprock material in time revealed another important aspect  
471 when anhydrous CO<sub>2</sub> is in contact with the water saturated sample; the pore water evaporates in the  
472 anhydrous CO<sub>2</sub> causing further dessication of the material that starts fissuring. Fissures, whether pre-  
473 existing in the material or new ones, play an important role on the CO<sub>2</sub>/caprock interaction. They  
474 drive most of the volumetric and hydraulic phenomena; swelling, desaturation, uptake, breakthrough.  
475 Their impact is still not well understood, in particular under realistic field conditions.

476 The long-term impact of CO<sub>2</sub> on the micro-structure of the shaly material is for the first time  
477 visualised with x-ray tomography on a solid sample and under non-extreme temperature and pressure  
478 conditions. Calcite dissolution is identified in carbonate-rich zones that after 9 months of exposure  
479 they were fissured (CM coupling). The mineralogical composition of these denser (white) inclusions  
480 in the x-ray images has been confirmed from SEM-EDX measurements. Segmentation and labelling  
481 the inclusions before and after long-duration CO<sub>2</sub> exposure confirmed an increased number of in-  
482 clusions due to breakage (dissolution) the mean orientation of which did not significantly evolve. A  
483 similar analysis has been made on the fissure network in the clay matrix of the sample before and  
484 after long-term exposure. The principal crack orientation in the sample is initially parallel to the  
485 bedding orientation of the shaly material. These fissures close with the application of confinement  
486 as shown in (Stavropoulou and Laloui, 2022) but very interestingly they do not re-appear 9 months  
487 later after pressure release. This result demonstrates the self-sealing response of Opalinus Clay (HM  
488 coupling). In addition to the closure of pre-existing fissures, the 9 months x-ray scan revealed the  
489 appearance of some new micro-fissures in the clay matrix (other than the fissures in the calcite zones)  
490 surprisingly in a perpendicular direction to the bedding. This aspect of potential re-arrangement of  
491 the fissure network of the material is demonstrated for the first time and could be due to additional  
492 chemo-mechanical mechanisms within the clay matrix or related to CO<sub>2</sub> breakthrough that due to



493 self-sealing of the initial micro-fissures initiated a new optimal pathway throughout the sample.  
 494 Finally, the CO<sub>2</sub> uptake in the caprock material has been investigated by combining the calculated  
 495 strain fields and the GV variation of the acquired x-ray images. CO<sub>2</sub> penetration in the sample has  
 496 been identified two months after initial exposure. It is hard to interpret the multi-phase fluid interac-  
 497 tion in the porous space of the material prior to two months due to the multiple THMC phenomena  
 498 that take place simultaneously and often counteract each other. It is interesting to note that after  
 499 CO<sub>2</sub> release the density of the sample remained increased compared to the initial two months earlier,  
 500 revealing potential CO<sub>2</sub> trapping in the material.

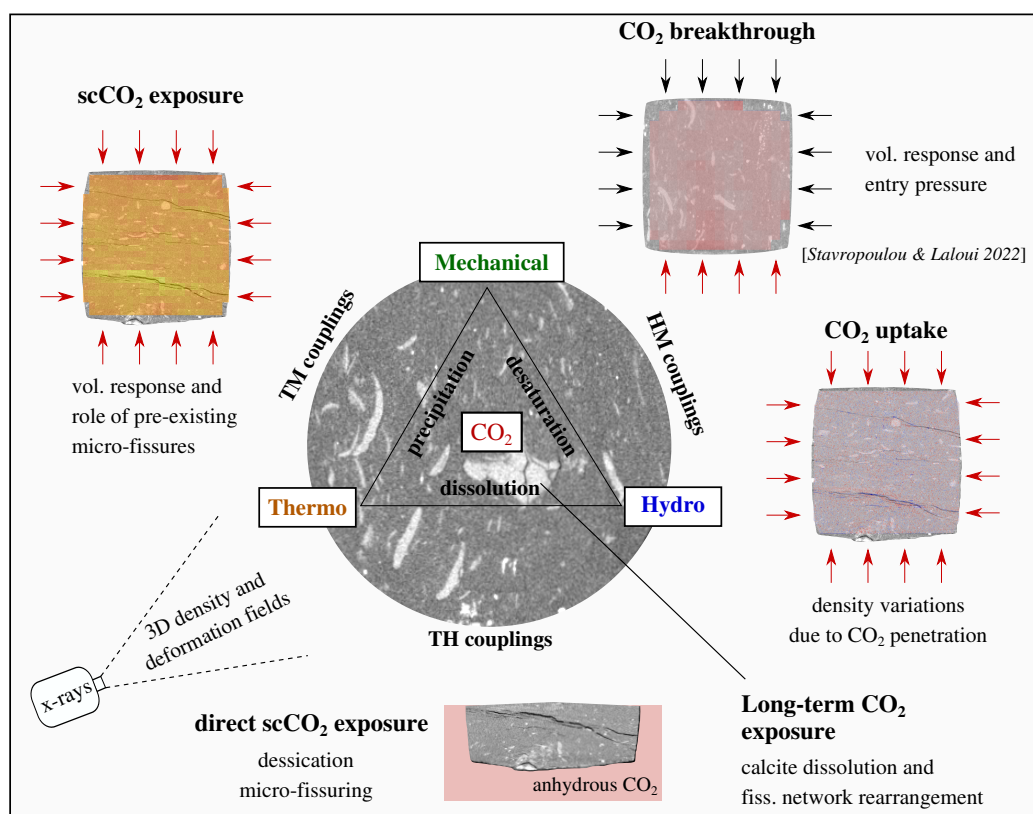


Figure 10: Coupled THMC mechanisms studied with *in-situ* x-ray imaging on small size shale samples

501 Figure 10 sums up the different coupled mechanisms that have been identified in this work to  
 502 occur during the CO<sub>2</sub>/caprock interaction. These topics require undoubtedly further investigation  
 503 with long-term experiments under continuously monitored conditions. Analysis of the response using





504 a non destructive tool, *i.e.* x-ray tomography allows the study of the material while under realistic  
505 conditions. The study of small shale samples has significantly contributed to the better understand-  
506 ing of the various coupled phenomena, first by achieving better time resolutions under non extreme  
507 temperature and pressure conditions, and then by studying the material's response under high spa-  
508 tial resolutions in 3D that revealed mechanisms previously undetectable with conventional testing  
509 methods and resolutions.

## 510 **6 Data availability**

511 The 3D x-ray images that have been used in this paper are provided online in Zenodo [link TBC].  
512 Additional data or results can be provided by the Authors upon reasonable request.

## 513 **7 Acknowledgements**

514 This study has taken place in the frame of the Spark SNSF CRSK-2\_196559 project. The Authors  
515 wish to thank the PIXE platform (EPFL) for the assistance during the x-ray tomography scans, as  
516 well as the Mont Terri laboratory and SwissTopo for providing the tested Opalinus Clay material.



## 517 Appendix A: Normalisation of x-ray tomographies

518 For the analysis of the attenuation evolution of the images, the different scans are normalised using  
 519 always as reference scan 00. The objective of this normalisation is to set to zero the voxels that  
 520 correspond to void in order to be able to more reliably detect density variations. The normalisation is  
 521 performed considering the parts of the image that are not supposed to vary in density with time; PEEK  
 522 and Aluminium. Since the void attenuation is changing with the introduction of CO<sub>2</sub>, the ratio of the  
 523 greyvalues (GV) between Aluminium, PEEK and air is considered constant as shown in Figure A1.

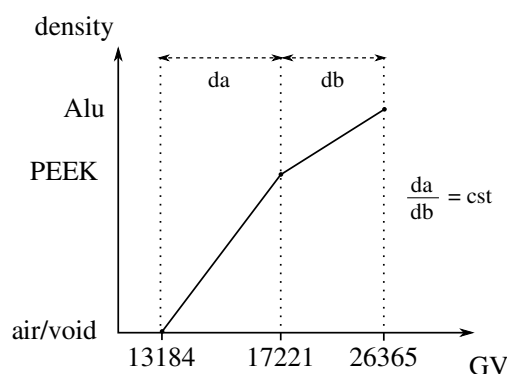


Figure A1: Measured greyvalues as a function of corresponding density in scan 00

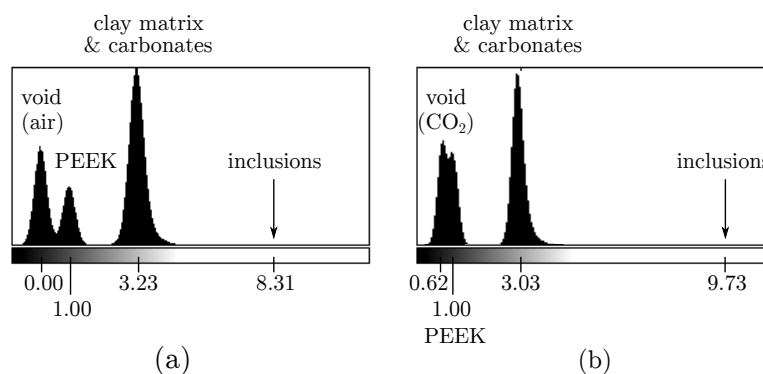
| GV (32b) | Void           | PEEK           | Aluminium      | da          | db   | da/db   |
|----------|----------------|----------------|----------------|-------------|------|---------|
| 00       | 13184<br>(832) | 17221<br>(833) | 26365<br>(900) | 4037        | 9144 | 0.44149 |
| 01       | <b>13113</b>   | 17195<br>(841) | 26442<br>(910) | <b>4082</b> | 9247 | 0.44149 |
| 02       | <b>13191</b>   | 17237<br>(839) | 26403<br>(907) | <b>4046</b> | 9166 | 0.44149 |
| 03       | <b>13450</b>   | 17330<br>(613) | 26119<br>(693) | <b>3880</b> | 8789 | 0.44149 |
| 04       | <b>13445</b>   | 17287<br>(602) | 25990<br>(699) | <b>3842</b> | 8703 | 0.44149 |

Table A1: Measured (normal font) and calculated (bold font) mean greyvalues (and standard deviation/error in the parenthesis) of the parts of the scan that are not expected to vary in density with time for the normalisation of the images

524 This ratio is calculated from the reference scan 00 (first row of Table A1) and considered constant



525 in order to deduce the air greyvalue of the rest of the scans. The computed GV of air (first column of  
526 Table A1) is then subtracted from each scan, which is then divided by the corresponding PEEK value  
527 so that PEEK average value is 1 for the sake of simplicity. The histogram of scan 00 after normali-  
528 sation is shown in Figure A2-a, while the histogram after CO<sub>2</sub> introduction (scan 003) is changed to  
529 that in Figure A2-b. The GV normalisation of the different scans can improve the volumetric analysis  
530 (DVC) and it is indispensable for the detection of density variations.



A2: Greyvalues histogram of normalised (a) scan 00 (no CO<sub>2</sub>) and (b) scan 01 (with CO<sub>2</sub>)

## 531 **Appendix B: Segmentation of the x-ray images**

532 The different steps for the segmentation for the different types of phases are illustrated in Figure B1.  
533 First, a bilateral filter is applied on the original image in order to smoothen the zones of similar phases  
534 and sharpen the edges between different phases (Figure B1-a).

535 The distributions of the GV levels before and after the application of this filter are plotted in  
536 Figure B2; a more narrow distribution is obtained after the bilateral filter, providing more precision for  
537 the selection of each GV range for the segmentation of the different phases. The resulted segmented  
538 slices of the inclusions and the micro-fissures after the application of a threshold GV range are shown  
539 in Figure B1-b and c, respectively. In the case of the inclusions, a double cycle of dilation and erosion  
540 of the binary image has been applied in order to reduce noise. This is not possible for a further  
541 reduction of the noise of the fissures' segmented image due to their 1 pixel thickness.

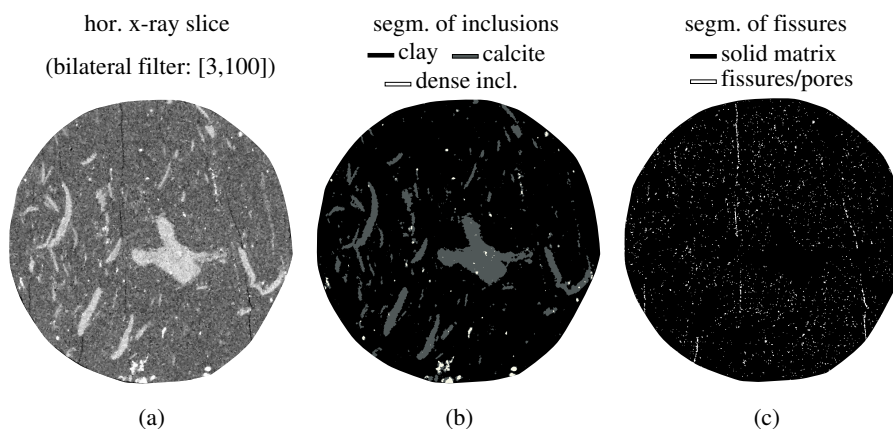
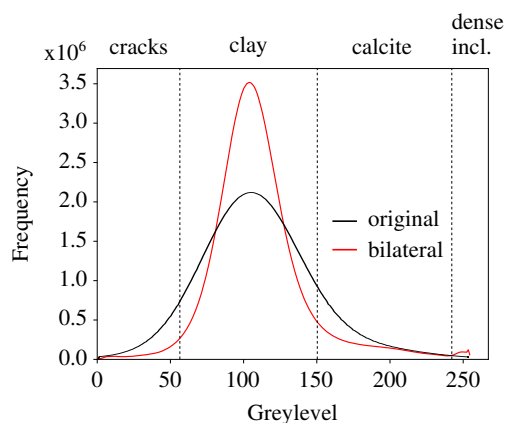


Figure B1: Horizontal slices after the (a) application of a bilateral filter, (b) segmentation of the two types of inclusions (calcite and denser inclusions), (c) micro-fissures



B2: Greyvalues histogram of the original horizontal x-ray slice and after the application of bilateral filter of Figure B2 (a)

## 542 References

- 543 [1] Alemu, B. L., Aagaard, P., Munz, I. A., & Skurtveit, E.: Caprock interaction with CO<sub>2</sub>: A  
 544 laboratory study of reactivity of shale with supercritical CO<sub>2</sub> and brine. *Applied Geochemistry*,  
 545 26(12), 1975-1989, <https://doi.org/10.1016/j.apgeochem.2011.06.028>, 2011.
- 546 [2] Amann-Hildenbrand, A., Bertier, P., Busch, A., & Krooss, B. M.: Experimental investigation  
 547 of the sealing capacity of generic clay-rich caprocks. *International Journal of Greenhouse Gas*  
 548 *Control*, 19, 620-641, <https://doi.org/10.1016/j.ijggc.2013.01.040>, 2013



- 549 [3] Armitage, P. J., Worden, R. H., Faulkner, D. R., Aplin, A. C., Butcher, A. R., & Iliffe, J.: Di-  
550 agenetic and sedimentary controls on porosity in Lower Carboniferous fine-grained lithologies,  
551 Krechba field, Algeria: A petrological study of a caprock to a carbon capture site. *Marine and*  
552 *Petroleum Geology*, 27(7), 1395-1410, [https://doi.org/10.1016/j.marpetgeo.2010.03.](https://doi.org/10.1016/j.marpetgeo.2010.03.018)  
553 018, 2010.
- 554 [4] Armitage, P.J., Faulkner, D.R., & Worden, R.H.: Caprock corrosion. *Nat. Geosci.*, 6, 79–80,  
555 2013.
- 556 [5] Bedford, J., Fousseis, F., Leclère, H. Wheeler, J., & Faulkner, D.: A 4D view on the evolution of  
557 metamorphic dehydration reactions. *Scientific Reports*, 7(1), 1-7. [https://doi.org/10.1038/](https://doi.org/10.1038/s41598-017-07160-5)  
558 [s41598-017-07160-5](https://doi.org/10.1038/s41598-017-07160-5), 2017.
- 559 [6] Birmipilis, G., Hall, S. A., Lages, S., & Dijkstra, J.: Monitoring of the nano-structure re-  
560 sponse of natural clay under mechanical perturbation using small angle X-ray scattering and  
561 digital image correlation. *Acta Geotechnica*, 14(6), 1965-1975, [https://doi.org/10.1007/](https://doi.org/10.1007/s11440-019-00832-8)  
562 [s11440-019-00832-8](https://doi.org/10.1007/s11440-019-00832-8), 2019.
- 563 [7] Birmipilis, G., & Dijkstra, J.: Testing sensitive clays through time and length scales. *IOP Con-*  
564 *ference Series: Earth and Environmental Science*, 710, 012021, [https://doi.org/10.1088/](https://doi.org/10.1088/1755-1315/710/1/012021)  
565 [1755-1315/710/1/012021](https://doi.org/10.1088/1755-1315/710/1/012021), 2021.
- 566 [8] Birmipilis, G., Andò, E., Stamati, O., Hall, S. A., Gerolymatou, E., & Dijkstra, J.: Experimental  
567 quantification of 3D deformations in sensitive clay during stress-probing, *Géotechnique*, 1-12,  
568 <https://doi.org/10.1680/jgeot.21.00114>, 2022.
- 569 [9] Bossart, P. & Thury, M.: Characteristics of the Opalinus clay at Mont Terri, Reports of the Swiss  
570 Geological Survey 3, 2011.
- 571 [10] Busch, A., Alles, S., Gensterblum, Y., Prinz, D., Dewhurst, D. N., Raven, M. D., Stanjek, H.,  
572 & Krooss, B. M.: Carbon dioxide storage potential of shales, *International journal of greenhouse*  
573 *gas control*, 2(3), 297-308, <https://doi.org/10.1016/j.ijggc.2008.03.003>, 2008.



- 574 [11] Crisci, E., Ferrari, A., Giger, S. B., & Laloui, L.: Hydro-mechanical behaviour of shallow Opal-  
575 inus Clay shale, *Engineering Geology*, 251, 214-227, [https://doi.org/10.1016/j.enggeo.](https://doi.org/10.1016/j.enggeo.2019.01.016)  
576 2019.01.016, 2019.
- 577 [12] Delage, P., & Tessier, D.: Macroscopic effects of nano and microscopic phenomena in clayey  
578 soils and clay rocks, *Geomechanics for Energy and the Environment*, 27, 100177, [https://doi.](https://doi.org/10.1016/j.gete.2019.100177)  
579 [org/10.1016/j.gete.2019.100177](https://doi.org/10.1016/j.gete.2019.100177), 2021.
- 580 [13] Delage, P., & Belmokhtar, M.: Drained triaxial testing of shales: insight from the Opalinus Clay,  
581 *Acta Geotechnica*, 17(7), 2855-2874, 2022.
- 582 [14] Desbois, G., Höhne, N., Urai, J. L., Bésuelle, P., & Viggiani, G.: Deformation in cemented  
583 mudrock (Callovo-Oxfordian Clay) by microcracking, granular flow and phyllosilicate plasticity:  
584 insights from triaxial deformation, broad ion beam polishing and scanning electron microscopy,  
585 *Solid Earth*, 8(2), 291, <https://doi.org/10.5194/se-8-291-2017>, 2017.
- 586 [15] Elkady, Y., & Kovscek, A. R.: Multiscale study of CO<sub>2</sub> impact on fluid transport and carbonate  
587 dissolution in Utica and Eagle Ford shale, *Journal of Petroleum Science and Engineering*, 195,  
588 107867, <https://doi.org/10.1016/j.petrol.2020.107867>, 2020.
- 589 [16] Espinoza, D. N., Kim, S. H., & Santamarina, J. C.: CO<sub>2</sub> geological storage - Geotechnical  
590 implications, *KSCE Journal of Civil Engineering*, 15(4), 707-719, [https://doi.org/10.1007/](https://doi.org/10.1007/s12205-011-0011-9)  
591 [s12205-011-0011-9](https://doi.org/10.1007/s12205-011-0011-9), 2011.
- 592 [17] Favero, V., Ferrari, A., & Laloui, L.: On the hydro-mechanical behaviour of remoulded and  
593 natural Opalinus Clay shale, *Engineering Geology*, 208, 128-135, [https://doi.org/10.1016/](https://doi.org/10.1016/j.enggeo.2016.04.030)  
594 [j.enggeo.2016.04.030](https://doi.org/10.1016/j.enggeo.2016.04.030), 2016.
- 595 [18] Favero, V., Ferrari, A., & Laloui, L.: Thermo-mechanical volume change behaviour of Opalinus  
596 Clay, *International Journal of Rock Mechanics and Mining Sciences*, 90, 15-25, [https://doi.](https://doi.org/10.1016/j.ijrmms.2016.09.013)  
597 [org/10.1016/j.ijrmms.2016.09.013](https://doi.org/10.1016/j.ijrmms.2016.09.013), 2016.
- 598 [19] Favero, V., & Laloui, L.: Impact of CO<sub>2</sub> injection on the hydro-mechanical behaviour of a clay-  
599 rich caprock, *International Journal of Greenhouse Gas Control*, 71, 133-141, [https://doi.org/](https://doi.org/10.1016/j.ijggc.2018.02.017)  
600 [10.1016/j.ijggc.2018.02.017](https://doi.org/10.1016/j.ijggc.2018.02.017), 2018.



- 601 [20] Hadian, P., & Rezaee, R.: The Effect of Supercritical CO<sub>2</sub> on Shaly Caprocks, *Energies*, 13(1),  
602 149, <https://doi.org/10.3390/en13010149>, 2020.
- 603 [21] Hashemi, S. S., & Zoback, M. D.: Permeability evolution of fractures in shale in the presence  
604 of supercritical CO<sub>2</sub>, *Journal of Geophysical Research: Solid Earth*, 126(8), e2021JB022266,  
605 <https://doi.org/10.1029/2021JB022266>, 2021.
- 606 [22] Houben, M. E., Desbois, G., & Urai, J. L.: Pore morphology and distribution in the Shaly  
607 facies of Opalinus Clay (Mont Terri, Switzerland): Insights from representative 2D BIB–SEM  
608 investigations on mm to nm scale, *Applied clay science*, 71, 82-97., [https://doi.org/10.](https://doi.org/10.1016/j.clay.2012.11.006)  
609 [1016/j.clay.2012.11.006](https://doi.org/10.1016/j.clay.2012.11.006), 2013.
- 610 [23] IPCC: *Climate Change 2022: Mitigation of Climate Change*, Contribution of Working Group  
611 III to the Sixth Assessment Report of the Intergovernmental Panel on Climate Change, Cam-  
612 bridge University Press, Cambridge, UK and New York, NY, USA. [https://doi.org/10.](https://doi.org/10.1017/9781009157926)  
613 [1017/9781009157926](https://doi.org/10.1017/9781009157926), 2022.
- 614 [24] Jia, Y., Lu, Y., Elsworth, D., Fang, Y., & Tang, J.: Surface characteristics and permeability  
615 enhancement of shale fractures due to water and supercritical carbon dioxide fracturing, *Journal*  
616 *of Petroleum Science and Engineering*, 165, 284-297, [https://doi.org/10.1016/j.petrol.](https://doi.org/10.1016/j.petrol.2018.02.018)  
617 [2018.02.018](https://doi.org/10.1016/j.petrol.2018.02.018), 2018.
- 618 [25] Kivi, I. R., Makhnenko, R. Y., & Vilarrasa, V.: Two-Phase Flow Mechanisms Controlling CO<sub>2</sub>  
619 Intrusion into Shaly Caprock, *Transport in Porous Media*, 141(3), 771-798, [https://doi.org/](https://doi.org/10.1007/s11242-022-01748-w)  
620 [10.1007/s11242-022-01748-w](https://doi.org/10.1007/s11242-022-01748-w), 2022.
- 621 [26] Li, C., & Laloui, L.: Impact of material properties on caprock stability in CO<sub>2</sub> geological stor-  
622 age, *Geomechanics for Energy and the Environment*, 11, 28-41, [https://doi.org/10.1016/](https://doi.org/10.1016/j.gete.2017.06.003)  
623 [j.gete.2017.06.003](https://doi.org/10.1016/j.gete.2017.06.003), 2017.
- 624 [27] Makhnenko, R. Y., Vilarrasa, V., Mylnikov, D., & Laloui, L.: Hydromechanical aspects of CO<sub>2</sub>  
625 breakthrough into clay-rich caprock, *Energy Procedia*, 114, 3219-3228, [https://doi.org/10.](https://doi.org/10.1016/j.egypro.2017.03.1453)  
626 [1016/j.egypro.2017.03.1453](https://doi.org/10.1016/j.egypro.2017.03.1453), 2017.



- 627 [28] Marschall, P., Horseman, S., & Gimmi, T.: Characterisation of gas transport properties of the  
628 Opalinus Clay, a potential host rock formation for radioactive waste disposal, *Oil & gas science  
629 and technology*, 60(1), 121-139, <https://doi.org/10.2516/ogst:2005008>, 2005.
- 630 [29] Menaceur, H., Delage, P., Tang, A. M., & Conil, N.: On the thermo-hydro-mechanical  
631 behaviour of a sheared Callovo-Oxfordian claystone sample with respect to the EDZ be-  
632 haviour, *Rock Mechanics and Rock Engineering*, 49(5), 1875-1888, [https://doi.org/10.  
633 1007/s00603-015-0897-5](https://doi.org/10.1007/s00603-015-0897-5), 2016.
- 634 [30] Minardi, A., Stavropoulou, E., Kim, T., Ferrari, A., & Laloui, L.: Experimental assessment of  
635 the hydro-mechanical behaviour of a shale caprock during CO<sub>2</sub> injection, *International Journal of  
636 Greenhouse Gas Control*, 106, 103225, <https://doi.org/10.1016/j.ijggc.2020.103225>,  
637 2021.
- 638 [31] Mohajerani, M., Delage, P., Sulem, J., Monfared, M., Tang, A. M., & Gatmiri, B.: The ther-  
639 mal volume changes of the Callovo–Oxfordian claystone, *Rock mechanics and rock engineering*,  
640 47(1), 131-142, <https://doi.org/10.1007/s00603-013-0369-8>, 2014.
- 641 [32] Prakash, R., Nguene, P.C.K., Noshadravan, A., & Abedi, S.: Chemical reactions of carbonate-  
642 rich mudstones with aqueous CO<sub>2</sub> and their impacts on rock's local microstructural and chemo-  
643 mechanical properties, *Journal of Natural Gas Science and Engineering*, 103, 104587, [https:  
644 //doi.org/10.1016/j.jngse.2022.104587](https://doi.org/10.1016/j.jngse.2022.104587), 2022.
- 645 [33] Romero, E.: Controlled-suction techniques. 4o Simpósio Brasileiro de Solos Não Saturados.  
646 Gehling & F. Schnaid (eds.), Porto Alegre, Brasil, 535-542, 2021.
- 647 [34] Rutqvist, J.: The geomechanics of CO<sub>2</sub> storage in deep sedimentary formations.  
648 *Geotechnical and Geological Engineering*, 30(3), 525-551, [https://doi.org/10.1007/  
649 s10706-011-9491-0](https://doi.org/10.1007/s10706-011-9491-0), 2012.
- 650 [35] Sciandra, D., Vilarrasa, V., Rahimzadeh Kivi, I., Makhnenko, R., Nussbaum, C., & Rebscher,  
651 D.: Coupled HM modeling assists in designing CO<sub>2</sub> long-term periodic injection experiment  
652 (CO<sub>2</sub>LPIE) in Mont Terri rock laboratory, In *EGU General Assembly Conference Abstracts* (pp.  
653 EGU21-8982), <https://doi.org/10.5194/egusphere-egu21-8982>, 2021





- 654 [36] Stamati, O., Andò, E., Roubin, E., Cailletaud, R., Wiebicke, M., et al.: spam: Software for  
655 Practical Analysis of Materials, *Journal of Open Source Software*, *Open Journals*, 5 (51), pp.2286,  
656 <https://doi.org/10.21105/joss.02286>, 2020. .
- 657 [37] Stavropoulou, E., Andò, E., Roubin, E., Lenoir, N., Tengattini, A., Briffaut, M., & Bésuelle, P.:  
658 Dynamics of water absorption in Callovo-Oxfordian claystone revealed with multimodal x-ray  
659 and neutron tomography, *Frontiers in Earth Science*, 8, 6, [https://doi.org/10.3389/feart.](https://doi.org/10.3389/feart.2020.00006)  
660 2020.00006, 2020
- 661 [38] Stavropoulou, E., & Laloui, L.: Evaluating CO2 breakthrough in a shaly a caprock material:  
662 a multi-scale experimental approach. *Scientific Reports*, 12(1), 1-19, [https://doi.org/10.](https://doi.org/10.1038/s41598-022-14793-8)  
663 1038/s41598-022-14793-8, 2022.
- 664 [39] Vego, I., Tengattini, A., Andò, E., Lenoir, N., & Viggiani, G.: Effect of high relative humidity  
665 on a network of a water-sensitive particles (couscous) as revealed by in-situ x-ray tomography,  
666 *Soft Matter*, <https://doi.org/10.1039/D2SM00322H>, 2022.
- 667 [40] Viggiani, G., & Hall, S. A.: Full-field measurements, a new tool for laboratory experimental  
668 geomechanics, In *Proceedings of the 4th Symposium on Deformation Characteristics of Geoma-*  
669 *terials*, 1, 3-26, 2008.
- 670 [41] Viggiani, G., Andò, E., Takano, D., & Santamarina, J. C.: Laboratory X-ray tomography: a  
671 valuable experimental tool for revealing processes in soils, *Geotechnical Testing Journal*, 38(1),  
672 61-71, <https://doi.org/10.1520/GTJ20140060>, 2015.
- 673 [42] Vilarrasa, V., Carrera, J., Olivella, S., Rutqvist, J., & Laloui, L.: Induced seismicity in geologic  
674 carbon storage, *Solid Earth*, 10(3), 871-892, <https://doi.org/10.5194/se-10-871-2019>,  
675 2019.
- 676 [43] Voltolini, M., & Ajo-Franklin, J. B.: The sealing mechanisms of a fracture in opalinus clay  
677 as revealed by in situ synchrotron x-ray micro-tomography, *Frontiers in Earth Science*, 8, 207,  
678 <https://doi.org/10.3389/feart.2020.00207>, 2020.
- 679 [44] Wang, L. L., Bornert, M., Chanchole, S., Yang, D. S., Héripré, E., Tanguy, A., & Calde-  
680 maison, D.: Micro-scale experimental investigation of the swelling anisotropy of the Callovo-



- 681 Oxfordian argillaceous rock, *Clay Minerals*, 48(2), 391-402, <https://doi.org/10.1180/>  
682 [claymin.2013.048.2.17](https://doi.org/10.1180/claymin.2013.048.2.17), 2013.
- 683 [45] Wang, S., & Tokunaga, T. K.: Capillary pressure–saturation relations for supercritical CO<sub>2</sub> and  
684 brine in limestone/dolomite sands: Implications for geologic carbon sequestration in carbonate  
685 reservoirs, *Environmental science & technology*, 49(12), 7208-7217, [https://doi.org/10.](https://doi.org/10.1021/acs.est.5b00826)  
686 [1021/acs.est.5b00826](https://doi.org/10.1021/acs.est.5b00826), 2015.
- 687 [46] Wollenweber, J., Alles, S., Busch, A., Krooss, B. M., Stanjek, H., & Littke, R.: Experimental  
688 investigation of the CO<sub>2</sub> sealing efficiency of caprocks, *International Journal of Greenhouse Gas*  
689 *Control*, 4(2), 231-241, <https://doi.org/10.1016/j.ijggc.2010.01.003>, 2010.
- 690 [47] Yang, K., Zhou, J., Xian, X., Zhou, L., Zhang, C., Tian, S., Lu, Z., & Zhang, F.: Chemical-  
691 mechanical coupling effects on the permeability of shale subjected to supercritical CO<sub>2</sub>-water  
692 exposure, *Energy*, 248, 123591, <https://doi.org/10.1016/j.energy.2022.123591>, 2022.
- 693 [48] Yasuhara, H., Kinoshita, N., Ohfuji, H., Lee, D. S., Nakashima, S., & Kishida, K.: Tem-  
694 poral alteration of fracture permeability in granite under hydrothermal conditions and its in-  
695 terpretation by coupled chemo-mechanical model, *Applied Geochemistry*, 26(12), 2074-2088,  
696 <https://doi.org/10.1016/j.apgeochem.2011.07.005>, 2021.
- 697 [49] Zappone, A., Rinaldi, A. P., Grab, M., Wenning, Q. C., Roques, C., Madonna, C., Obermann,  
698 A. C., Bernasconi, S. M., Brennwald, M. S., Kipfer, R., Soom, F., Cook, P., Guglielmi, Y.,  
699 Nussbaum, C., Giardini, D., Mazzotti, M., & Wiemer, S.: Fault sealing and caprock integrity for  
700 CO<sub>2</sub> storage: an in situ injection experiment, *Solid Earth*, 12, 319–343, [https://doi.org/10.](https://doi.org/10.5194/se-12-319-2021)  
701 [5194/se-12-319-2021](https://doi.org/10.5194/se-12-319-2021), 2021.